# Supplementary Materials for

## Highly efficient p-i-n perovskite solar cells that endure temperature variations

Guixiang Li, Zhenhuang Su, Laura Canil, Declan Hughes, Mahmoud H. Aldamasy, Janardan Dagar, Sergei Trofimov, Luyao Wang,* Weiwei Zuo, José J. Jerónimo-Rendon, Mahdi Malekshahi Byranvand, Chenyue Wang, Rui Zhu, Zuhong Zhang, Feng Yang, Giuseppe Nasti, Boris Naydenov, Wing C. Tsoi, Zhe Li, Xingyu Gao, Zhaokui Wang, Yu Jia, Eva Unger, Michael Saliba, Meng Li,* and Antonio Abate*

Correspondence to: mengli@henu.edu.cn (M.L.); luyao.wang@helmholtz-berlin.de (L.W.); antonio.abate@helmholtz-berlin.de (A.A.)

**This PDF file includes:**

       Materials and Methods
       Supplementary Text
       Figs. S1 to S39
       Tables S1 to S5
       References (*45–52*)

**Materials and Methods**

<u>Materials</u>

Organic salts of formamidinium iodide (FAI, 99.99%, trace elements basis) and methylammonium bromide (MABr, 99.99%, trace elements basis) were purchased from Dyenamo. Lead(II) iodide ($PbI_2$, 99.99%, trace metals basis) and lead(II) bromide ($PbBr_2$), as well as self-assembly molecule [2-(3,6-dimethoxy-9H-carbazol-9-yl)ethyl]phosphonic acid (MeO-2PACz, >98.0%) were purchased from TCI. Cesium iodide (CsI, 99.999%, AB 109298) and [6,6]-phenyl-$C_{61}$-butyric acid methyl ester ($PC_{61}BM$, product: OSO226) were provided by HySPRINT Helmholtz Innovation Lab and used without further purification. Bathocuproine (BCP, 99.8%) was acquired from Ossila and Silver shots (Ag, 2-3 mm, 99.999%) was bought from Alfa Aesar, respectively. Chlorobenzene (CB) and $\beta$-poly(1,1-difluoroethylene) ($\beta$-pV2F) were purchased from Sigma Aldrich. Dimethyl sulfoxide (DMSO) and *N,N*-dimethylformamide (DMF) were obtained from Creaphys GmbH. Mucasol solution for substrate cleaning was obtained from Schülke & Mayr GmbH. Besides, ethanol, acetone and 2-propanol (IPA) were used for further substrate cleaning as received from VWR International Ltd.

<u>Device Fabrication</u>

*Substrate Cleaning.* Patterned indium-doped tin oxide (ITO) glass substrates (25 mm x 25 mm, thickness of 80 nm) were firstly cleaned with 2% Mucasol solution dispersed in deionized water under ultrasonication for 15 min, followed by pure deionized water with 5 min ultrasonication. Subsequently, these substrates were sequentially cleaned by acetone and 2-propanol under ultrasonication for 15 min. After that, ITO glass substrates were dried with $N_2$ blowing and hot plate. Ultimately, we used UV-ozone to treat substrates for 30 min.

*Precursor Solution Preparation.* The perovskite precursor solution was prepared by dissolving 1.5 M triple-cation halide salts according to a formula of $Cs_{0.05}(FA_{0.98}MA_{0.02})_{0.95}Pb(I_{0.98}Br_{0.02})_3$ in the mixed solvent of DMF/DMSO (4:1 in *v:v*). Additionally, 0.5 mg/mL $\beta$-pV2F polymer molecule was dissolved in the DMF/DMSO solvent as the additive into the perovskite precursor. During this process, the mixed solutions were stirred overnight in a shaker with 60 °C. Resultant solutions were filtered through a 0.45 μm hydrophobic PTFE filter before use.

*Perovskite Solar Cell Fabrication.* The inverted p-i-n architecture perovskite solar cells (PSCs) in a planar system were fabricated through the following procedure. Typically, 100 μL MeO-2PACz (0.335 mg/mL) dissolved in absolute ethanol, as a hole transport material, was spin-coated on the ITO glass substrates using a speed of 3,000 rpm for 30 s with an acceleration of 500 rpm/s, followed by annealing at 100 °C for Subsequently, 100 μL perovskite precursor was applied into MeO-2PACz layer. The dispersed perovskite solution was spin-coated with 6000 rpm for 35 s with a ramp of 1000 rpm/s. At 10 s before the end of the procedure, 200 μL chlorobenzene as the antisolvent was dripped into the precast film surface. After that, the substrates were quickly transferred to a hot plate with 100 °C for 45 min annealing. Then, starting the program with 3000 rpm for 30 s with a ramp of 3000 rpm/s, 20 mg/mL $PC_{61}BM$ in chlorobenzene was spin-coated on the obtained perovskite layers after 3 s to acquire the electron selective contact. Sequentially, 8 nm BCP controlled by temperature and 100 nm Ag electrode via controlling power were thermally deposited on the $PC_{61}BM$ layer with a shadow mask, using a thin-film evaporation system under a high vacuum lower than $1 \times 10^{-6}$ mbar. Ultimately, the PSCs with defined areas of 18 mm² on

each pixel were obtained. In addition, the device with defined working area of 1 cm$^2$ was also fabricated by covering the large-area mask. Notably, the whole device fabrication process was carried out in distraction-free N$_2$-filled gloveboxes.

Characterization

*Performance Measurement.* Photocurrent-voltage (*J-V*) curves of PSCs under 1 sun equivalent illumination were recorded with a programmable Keithley 2400 source meter under a Wavelabs Sinus-70 LED class AAA sun simulator. The light intensity was calibrated using a filtered KG3 silicon reference solar cell from Fraunhofer-Institut für Solare Energiesysteme ISE. *J-V* scans were carried out with a step size of 0.02 V, monitored by a controllable measurement program written in LabView. Device performance metrics of $J_{sc}$, FF, $V_{oc}$ and PCE were collected from the *J-V* measurements. During the *J-V* measurements, PSCs employed defined device areas of 18 mm$^2$ and 1 cm$^2$. Also, the stabilized power outputs at the maximum power points (MPP) was tracked under illumination, where the PSCs were biased at the MPP voltage. The external quantum efficiency (EQE) spectra from 300 to 850 nm were collected by Oriel Instruments QEPVSI-b system integrated with Xenon arc lamp (Newport 300 W), which was controlled *via* TracQ-Basic software. The system was equipped with a chopper and the monochromatic light (Newport Cornerstone 260) for filtering the white light. Before measurements, the EQE setup was calibrated through a standard silicon photodetector with known spectral response. The operational stability of the unencapsulated devices is tested at the MPP tracking under simulated 1 sun illumination (LED solar simulator). The illumination intensity of the LED lamp is calibrated. There is an interval of 30 min for data collection. During the MPP tracking, the device is performed in an inert atmosphere at room temperature (25 °C). Thermal stability under elevated temperature is conducted at 75 °C in an inert atmosphere with continuous MPP tracking. The temperature-dependent test setup is mainly equipped with temperature and vacuum controllers, liquid nitrogen, vacuum pump, sample chamber, solar simulator. Specifically, temperature was controlled by hot and cold stage (HCP421V-PM), which is equipped with temperature controller (mK2000B), temperature control sensor (100 Ω Platinum RTD), liquid nitrogen cooling system, 3 L liquid nitrogen dewar (LN2-D3), water pump with heat exchanger, DC power supply, and temperature control software (Instec App). The inner sample chamber is cooled by the liquid nitrogen cooling accessory (INSTEC LN2-P). Setup temperature can range from −190 °C to 400 °C, with temperature stability of ±0.05 °C (>25 °C), ±0.1 °C (<25 °C). Maximum heating rate is +150 °C/min (at 37 °C), cooling rate is −50 °C/min (at 37 °C). Minimum heating and cooling rate is ±0.1 °C/h. During the operation, the device was placed in a chamber with controllable temperature and pressure. Liquid nitrogen was introduced to adjust the device temperature. During our thermal cycling, the temperature was controlled between −60 and +80 °C. For temperature ramps, we performed the WinTemp RAMP temperature (c) AT rate (°C/min) command to set up the ramp parameters in our experiments. The solar simulator with a 450 W xenon lamp (Sol3A Class AAA Solar Simulator, Oriel, USA) was used to record the device performance.

*Structure Characterization.* Field-emission scanning electron microscope (SEM) measurements were carried out on a Quanta 200 FEG (FESEM, FEI Co.) to investigate the morphology and thickness of perovskites by measuring top and cross-sectional views. Atomic force microscope (AFM) was employed to reveal the topographical features of perovskite films by a Park Systems NX12 equipment. AFM topographies were analyzed using the open-source software Gwyddion$^©$. Kelvin probe (KP) was implemented to measure the contact potential

difference (CPD). The KP setup was installed a vibrating gold mesh driven by a piezo electric crystal (Kelvin probe S and CPD controller from Besocke Delta Phi). X-ray diffraction (XRD) pattern was acquired by Panalytical Empyrean diffractometer with Cu Kα radiation. The synchrotron-based *in situ* grazing-incidence wide-angle X-ray scattering (GIWAXS) was conducted by the BL14B1 beamline at Shanghai Synchrotron Radiation Facility (SSRF). Corresponding X-ray beam possesses the wavelength of 1.24 Å at a grazing incidence angle of 0.3° and uses an energy of 10 KeV. Two-dimensional (2D) GIWAXS patterns were collected from a MarCCD 225 detector with a distance of 330 mm between samples and detector. The FIT2D software was employed to parse 2D GIWAXS patterns. GIWAXS patterns were presented in scattering vector $q$ coordinates based on the equation $q = 4\pi\sin\theta/\lambda$, where $\theta$ is the half of diffraction angle and $\lambda$ is the incident wavelength. In the processing of the GIWAXS data, the vector $q$ was calibrated by measuring XRD from a Lanthanum hexaboride reference sample. Fourier-transform infrared spectroscopy (FT-IR) spectra were recorded by a FT/IR-4100 (JASCO) spectrometer, equipped with a universal attenuated total reflectance module. The polymer powder sample was prepared by grinding with potassium bromide (KBr) to produce a pellet, where polymer powder was mixed with KBr. The sample with the applied layer was pressed to the surface of the attenuated total reflection diamond crystal of the spectrometer. The perovskite film on glass was prepared by being cut into a small piece, and then pressed to the surface of the attenuated total reflectance diamond crystal. Water contact angle measurements for perovskite films were analyzed using a JC000DI optical contact-measuring system. We also conducted damp tests on perovskite films by placing them in 50% humidity air for 18 h to examine the resilience of the perovskite against moisture degradation. Steady-state photoluminescence (PL) spectra were obtained from LabVIEW software with a lab-built PL setup, which was installed a reflectance probe and a fiber-optic spectrometer from Ocean Insight. The PL measurements were performed by entering an integrating sphere through optical fiber, where the integration time was 300 ms and a 532 nm pulsed laser was used as excitation source. The device operational stability under the thermal cycling condition was measured without any encapsulation. Time-of-flight secondary ion mass spectrometry (ToF-SIMS) measurements were conducted using TOF-SIMS 5-100 produced by ION-TOF GmbH. The aged completed devices by thermal cycling used a 30 keV Bi+ ion beam as the primary ion beam to peel the samples with an analysis area of $80 \times 80$ μm$^2$. For the sputtering, a Cs beam (500 eV) was performed to obtain the desired depth profile, where the sputtering areas were $230 \times 230$ μm$^2$ for devices measurement. During these measurements, negative ion mode was used. Secondary ion clusters or molecular ion signals of $Ag^-$, $C_{60}^-$, $I^-$, $AgI_2^-$, $PbI_3^-$, $CN_2H_5I^-$, $CF_2^-$, and $InO_2^-$ were recorded to track the Ag, PCBM, I, AgI, PbI$_2$, FAI, $\beta$-pV2F, and ITO species.

**Supplementary Text**

Hysteresis Index Calculation

The hysteresis index is calculated using the difference between forward-scan and reverse-scan efficiencies obtained from *J-V* curves, defined as (*45*):

$$\text{Hysteresis index} = \frac{PCE_{reverse} - PCE_{forward}}{PCE_{reverse}} \quad \text{(Equation 1)}$$

In this work, we used the same scan rate and range for all *J-V* curves for inverted and forwarded scans to avoid the operational influence.


Lattice Strain Calculation

For assessing the strain index $\sigma$ of perovskite lattices, we utilize the $2\theta$-$\sin^2\varphi$ method associated with Bragg's Law and generalized Hooke's Law, as (equation 2) (*39, 46*).

$$\sigma = \frac{E}{(1+v)\sin^2\varphi} \cdot \left(\frac{d_\varphi - d_n}{d_n}\right) \quad \text{(Equation 2)}$$

where $\varphi$ and $n$ are the scattering vector angles, pertaining to the perovskite film surface normal direction.

For the out-of-plane and in-plane directions, we obtain that out-of-plane $\varphi = 90°$ ($\perp$) and in-plane $n = 0°$ ($/\!/$). Then it can be calculated that $\sin^2\varphi = 1$, as shown in (equation 3).

$$\sigma = \frac{E}{(1+v)} \cdot \left(\frac{d_\perp - d_\|}{d_\|}\right) \quad \text{(Equation 3)}$$

Due to $q = 2\pi/d$, we further convert (equation 3) to (equation 4) as follows.

$$\sigma = \frac{E}{(1+v)} \cdot \left(\frac{q_\| - q_\perp}{q_\|}\right) \quad \text{(Equation 4)}$$

We introduce $\Delta q$ to represent the difference between $q_\|$ and $q_\perp$ ($\Delta q = q_\| - q_\perp$). Since the change in the denominator $q_\perp$ is negligible compared to that in the numerator $\Delta q$, we can use a constant value $q_0$ to represent, resulting as (equation 5).

$$\sigma = \frac{E}{q_0(1+v)} \cdot \Delta q \quad \text{(Equation 5)}$$

where $E$ is Young's modulus and $v$ is Poisson's ratio of the perovskite film, respectively. $E$ and $v$ are evaluated as 10 GPa and 0.3, respectively. Also, the scattering vector constant $q_0 = 10.12$ nm$^{-1}$ is available (*47–49*).

From the resultant (equation 5), we can observe that $\sigma$ is proportional to $\Delta q$ value. The $\Delta q$ is calculated by subtracting the out-of-plane scattering vector $q_z$ value from that ($q_y$) of in-plane.

**Supplementary Figures**
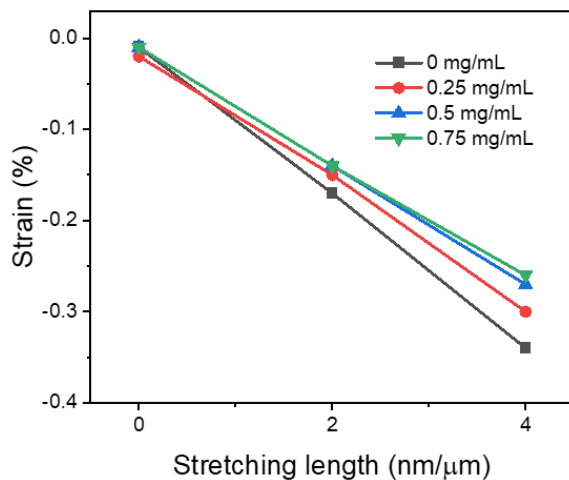


**Fig. S1.** The strain intensity as a function of stretching lengths. (The strain (%) is calculated by dividing the $q$ difference ($\Delta q$) by the $q$ value.)

We performed wide-angle X-ray scattering (WAXS) of the perovskite film while stretching them by 0, 2 and 4 nm/μm. The $\beta$-pV2F's introduction reduces the strain generation of perovskites during stretching. Among them, the increased concentrations of 0.5 mg/mL and 0.75 mg/mL show a minor deformation and lattice strain.
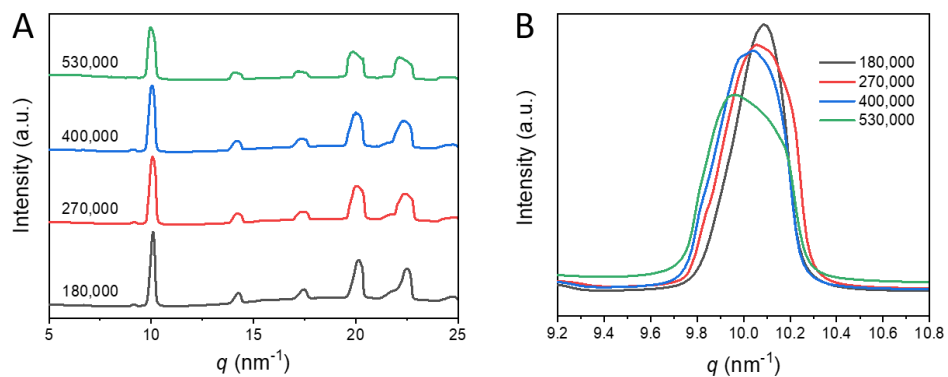
**Fig. S2.** Azimuth-integration 1D plots for perovskite films with polymer molecular weight of 180,000, 270,000, 400,000 and 530,000 g/mol.

From the synchrotron-based grazing-incidence wide-angle X-ray scattering (GIWAXS) results in **Fig. S2**, the 180,000 MW polymer-based perovskite has the strongest peak intensity and the smallest full width at half maximum (FWHM).
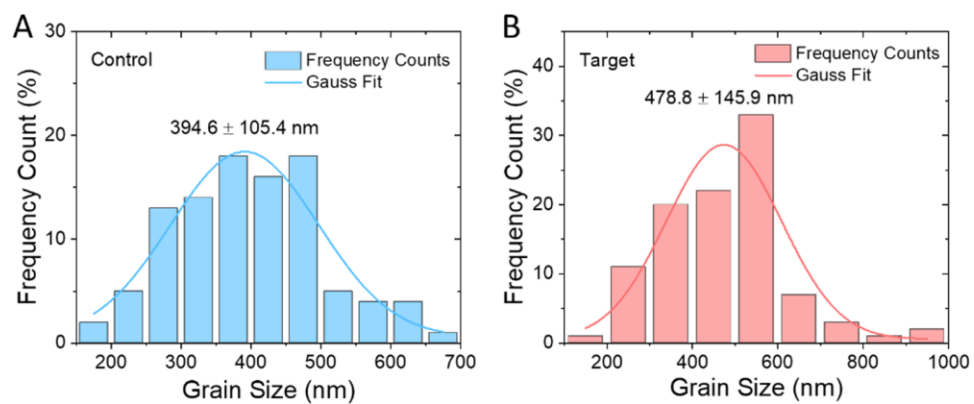
**Fig. S3.** Statistic grain size distribution histograms of (**A**) control and (**B**) target perovskite films.
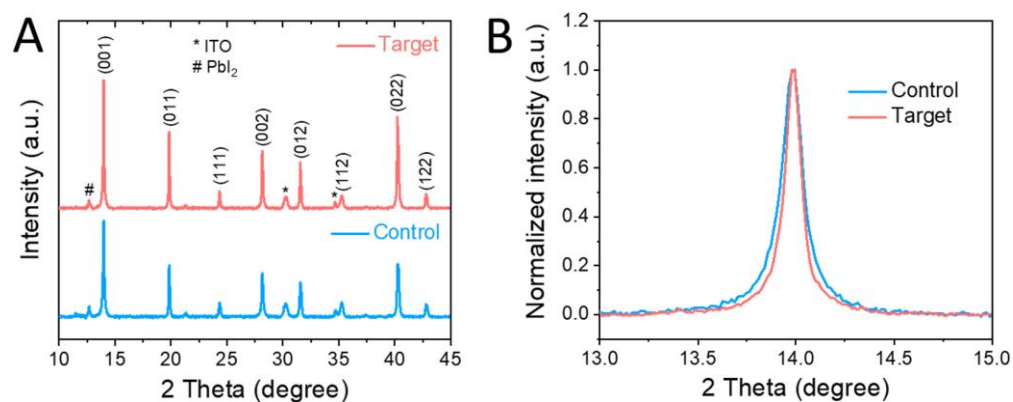
**Fig. S4.** The (**A**) XRD patterns and (**B**) FWHM of (001) diffraction peaks of control and target perovskite films.

The introduction of $\beta$-pV2F does not show a noticeable peak shift in X-ray diffraction (XRD) patterns (**Fig. S4A**), indicating that the $\beta$-pV2F molecules are not incorporated into the perovskite crystal lattice. The broadening of the XRD peak usually results from low crystalline quality, while the reduced FWHM extracted from **Fig. S4B** is observed in target perovskite, revealing an improved film quality (*15*).
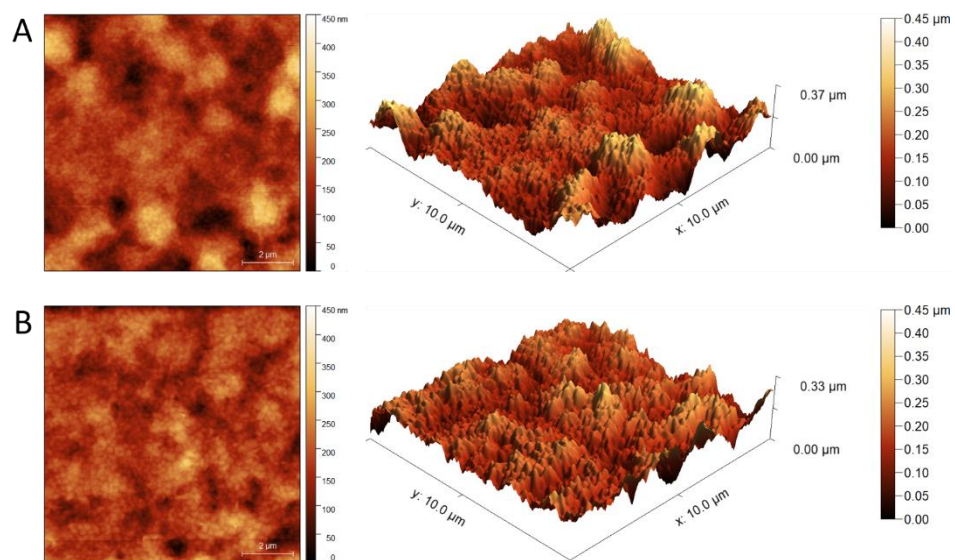
**Fig. S5.** AFM images of the surface morphologies of (**A**) control and (**B**) target perovskite films.

We employed atomic force microscope (AFM) to analyze the topographical features of perovskite films.
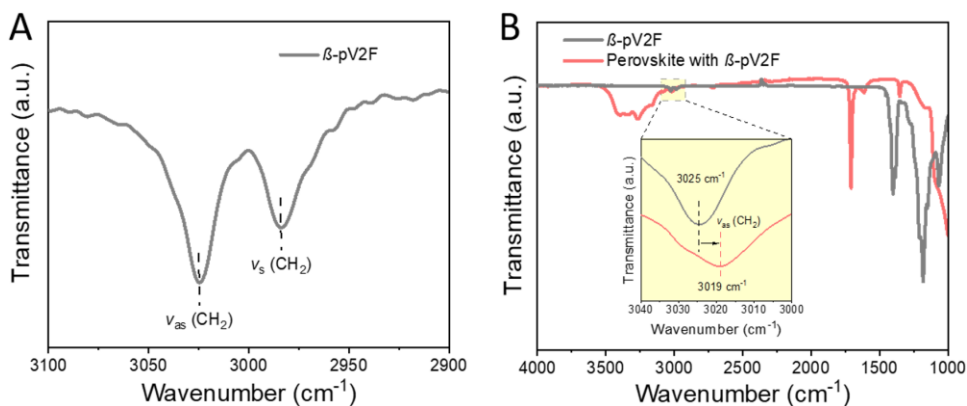
**Fig. S6.** The FT-IR spectra with fingerprint region of control and target perovskite films.

We conducted Fourier-transform infrared spectroscopy (FT-IR) measurements to verify the interaction between $\beta$-pV2F and perovskite. The FT-IR spectrum at the higher frequency region of 2900-3100 cm$^{-1}$ shows the asymmetric ($v_{as}$) and symmetric ($v_s$) stretching vibrational bands of $-CH_2$ groups in $\beta$-pV2F molecule (**Fig. S6A**). After that, we observe the position of $v_{as}$ band shifts from 3025 cm$^{-1}$ to 3019 cm$^{-1}$ for the perovskite film treated with $\beta$-pV2F compared to the pristine $\beta$-pV2F molecule (**Fig. S6B**). The result indicates an interaction between $-CH_2$ dipoles of $\beta$-pV2F and halide ions of $[PbX_6]^{4-}$ frame *via* C-H$\cdots$X dipole bonding (*50, 51*).
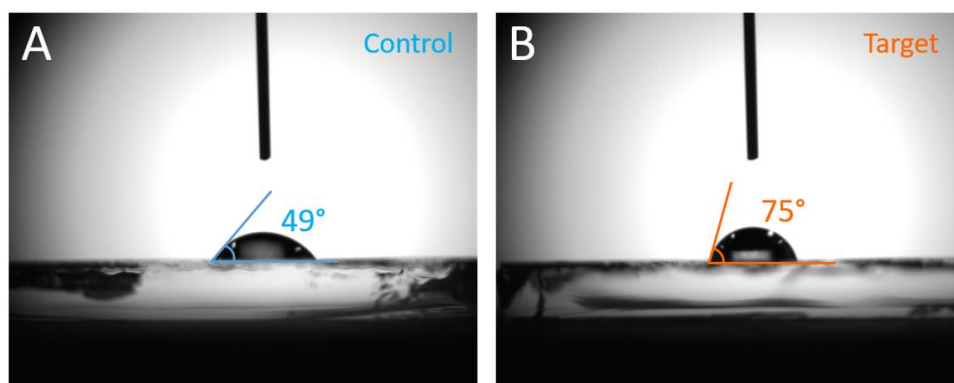
**Fig. S7.** The water contact angles of (**A**) control and (**B**) target perovskite films.

As the growth proceeds, the long-chain $\beta$-pV2F are partially expelled to the perovskite film surface, the enhanced hydrophobicity (**Fig. S7**).
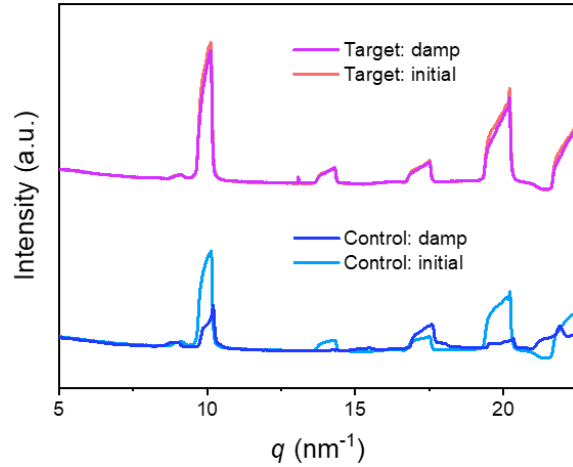
**Fig. S8.** GIWAXS profiles for perovskite films before and after damp tests (50% humidity air for 18 h).

**Fig. S8** shows that the control film exhibits a significant drop in the diffraction signal after being damp, while the target film retains the diffraction peaks close to its initial state. This result further confirms the enhanced film hydrophobicity against moisture degradation.
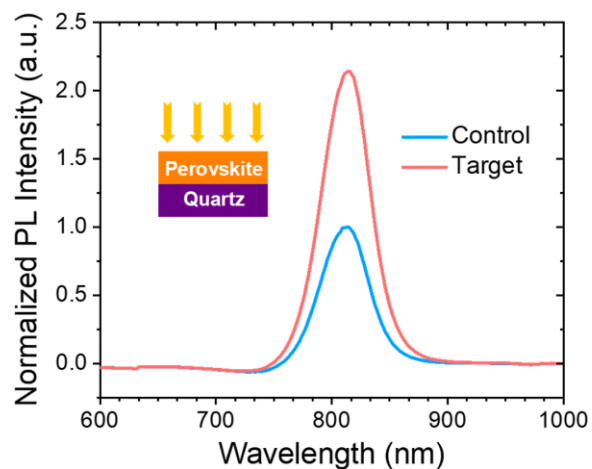
**Fig. S9.** Steady-state PL spectra for control and target perovskite thin films prepared on quartz substrates.

**Fig. S9** shows the enhanced photoluminescence (PL) intensity after introducing $\beta$-pV2F into perovskite, corresponding to a reduced defect-induced nonradiative recombination.
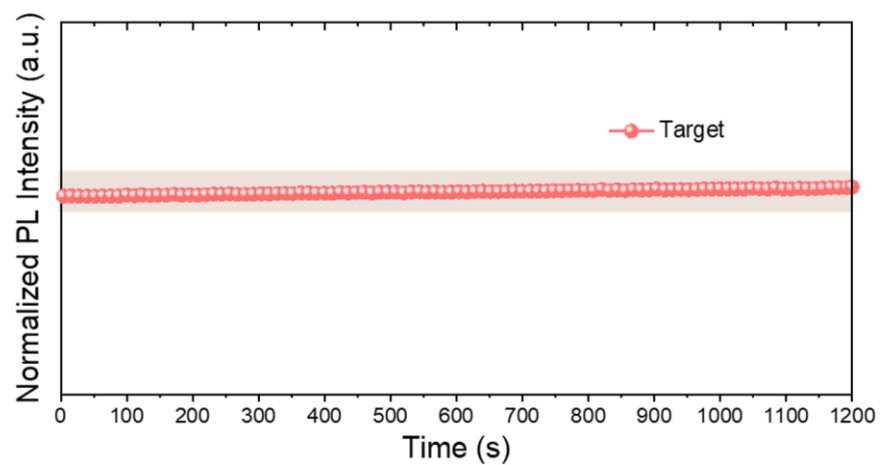
**Fig. S10.** The time dependent PL intensity of target perovskite film under continuous illumination.

Prolonging the illumination time to 1200 s does not lead to a decrease in the PL intensity (**Fig. S10**), suggesting that the $\beta$-pV2F-based perovskite films have excellent photostability for overcoming photoinduced defect generation.
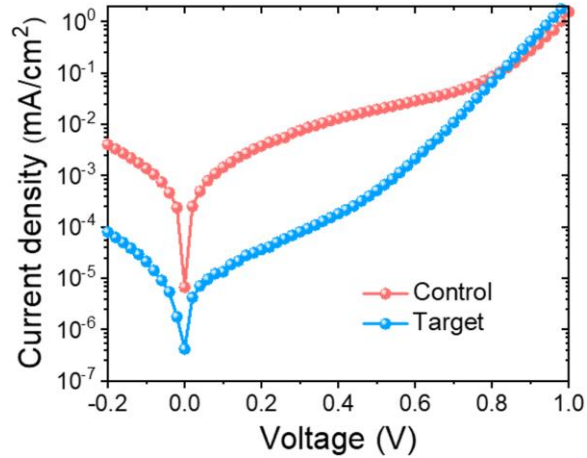
**Fig. S11.** Dark *J-V* characteristics of the control and target devices.

To find the cause for the reduced charge recombination, we carried out the dark current density-voltage (*J-V*) curves measurements for control and target devices. As displayed in **Fig. S11**, the dark current density of the target device is over an order of magnitude lower than that of the control device. It shows that the functionalization of *β*-pV2F suppresses the leakage current and the photogenerated carriers are effectively separated during the photoelectric conversion process (*22, 52*). This scenario allows the increase of the $V_{oc}$ in devices (*25, 26*).
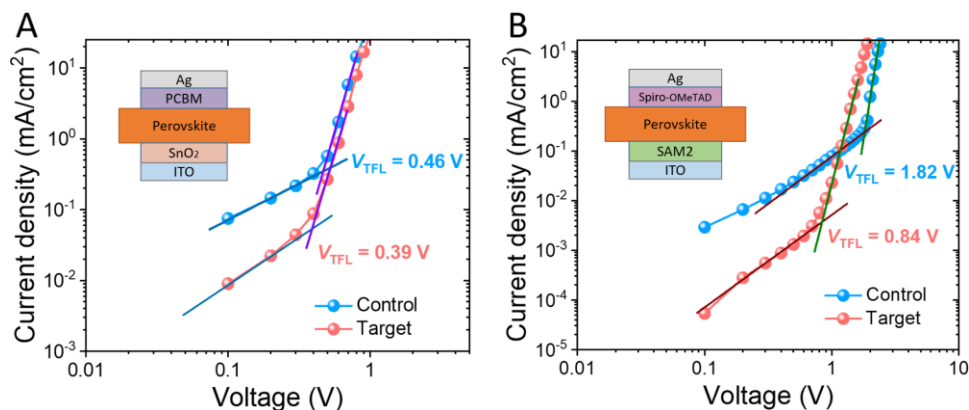
**Fig. S12.** SCLC curves of (**A**) electron-only and (**B**) hole-only control and target devices, respectively. The insets corresponds to the respective device structures.

The trap concentration is assessed by measuring space-charge-limited-current (SCLC) curves. It can be obtained that, from the dark *J-V* curves of electron-only devices in **Fig. S12A**, the trap-filled limit voltages ($V_{TFL}$) are 0.46 V for control and 0.39 V for target, respectively manifesting the lower electron trap density in target devices. Additionally, the less hole trap density for target devices is shown in **Fig. S12B**. These results confirm that the $\beta$-pV2F molecular functionalisation can eliminate trap states in the perovskite bulk and facilitate interfacial charge transfer (*21, 23*).
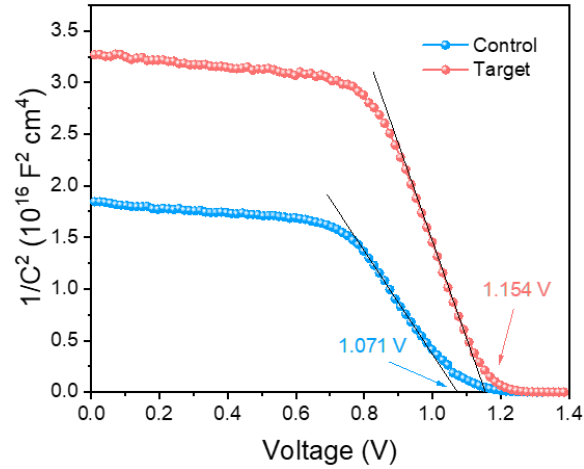
**Fig. S13.** Mott–Schottky plots of the devices without and with polymer treatment.

To further demonstrate the formation of the electric field, we conducted the Mott–Schottky analysis. As shown in **Fig. S13**, the built-in potential ($V_{bi}$) values of the control and target PSCs are 1.071 V and 1.154 V, respectively. The increased $V_{bi}$ indicates the formation of an interfacial electric field, resulting in fast charge collection and less carrier accumulation at the interface.
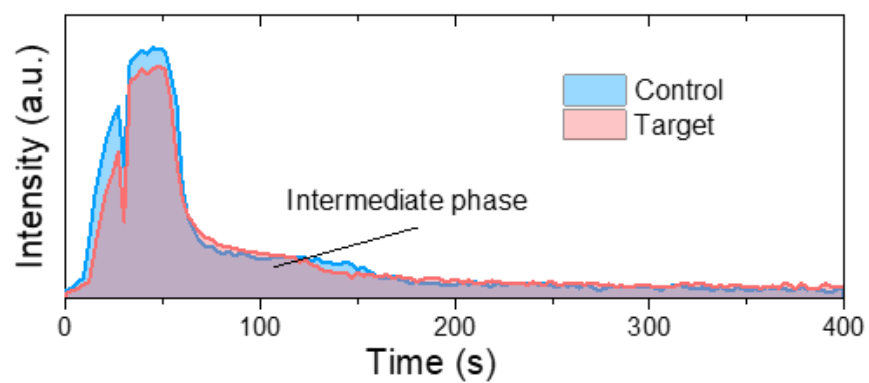
**Fig. S14.** Time-resolved integrated peak area intensity for intermediate phases of control and target perovskites.

The intensity fluctuations at 25 s in **Fig. S14** result from antisolvent dropwise.
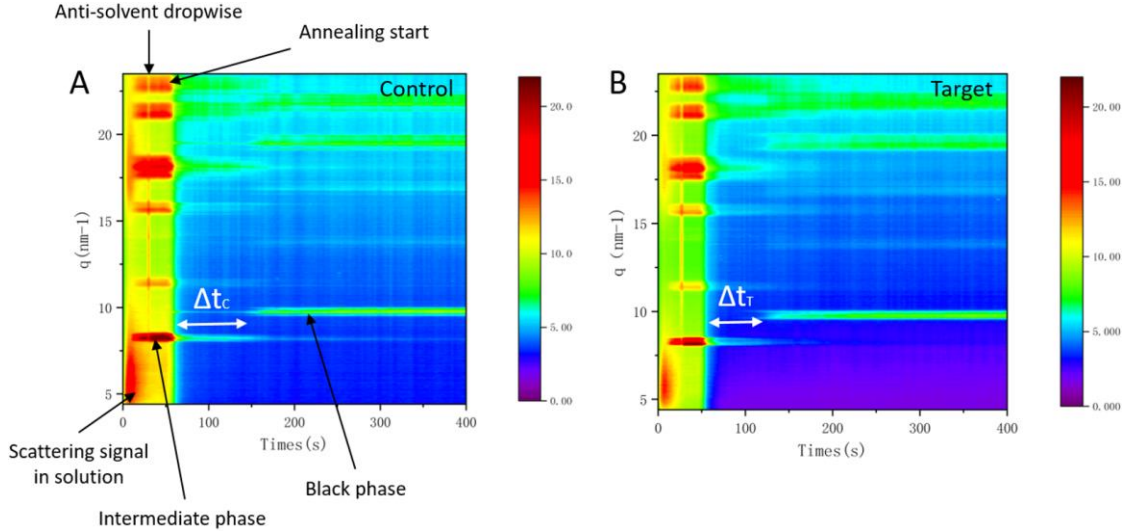
**Fig. S15.** The time-dependence X-ray scattering evolution during the (**A**) control and (**B**) target perovskite film formation process.

In GIWAXS intensity profiles, several different diffraction signals and stages are presented (**Fig. 2, A** and **B**, and **Fig. S15**). The initial $t_1$ stage (during the first 25 s) reveals the scattering halo at low $q$ values from 8 to 8.5 nm$^{-1}$ from the solvated colloidal sol precursor. The signal transition at $t_2$ (25 s) originates from the dripping of antisolvent. Subsequently, the supersaturated solvate intermediate emerges as shown at stage $t_3$, accompanied by the spin coating process, and this state is continuously maintained for a gap between the formation of solvate and perovskite crystals. When performing annealing stating at $t_4$ (around 60 s), we directly observe that the intermediate phase signal intensity gradually weakened, as presented $t_5$ stage. As time went by, the black phase centered at scattering vector $q = \sim 10$ nm$^{-1}$ along the (001) crystal plane comes into view by degrees at stage $t_6$. The almost only scattering feature observed in the cast film indicates that the colloid has solidified and converted into a black phase. Stage $t_7$ claims the cessation of further crystal growth. Finally, a larger ending window with uniform diffraction intensity can be observed.
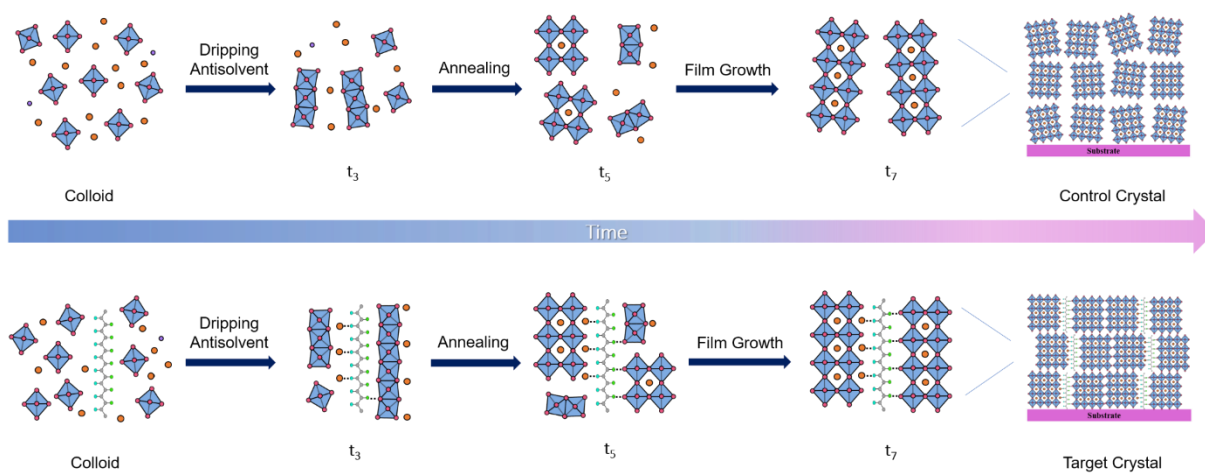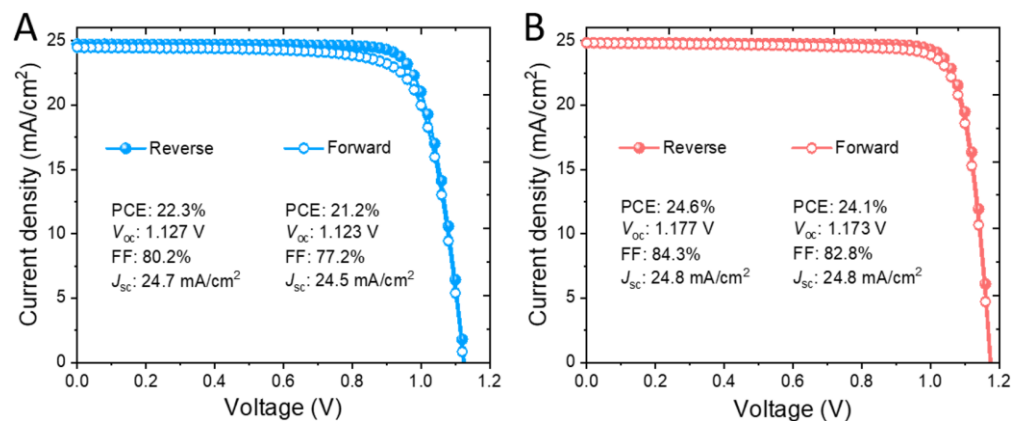
**Fig. S16.** The schematic diagram of crystallization kinetics.
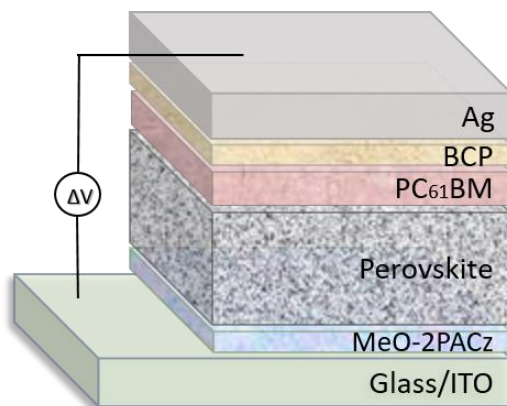
**Fig. S17.** Schematic device architecture of the inverted p-i-n PSCs.

The architecture of inverted p-i-n planar PSCs is constructed as glass/ ITO/ MeO-2PACz/ perovskite/ $PC_{61}BM$/ BCP/ Ag.

**Fig. S18.** *J-V* curves with the reverse and forward sweep for (**A**) control and (**B**) target devices.

The hysteresis factors of control and target PSCs are 4.9% and 2.0%, respectively (**Fig. S18**), thanks to reduced bulk defects and surface traps for charge recombination loss (*3*).
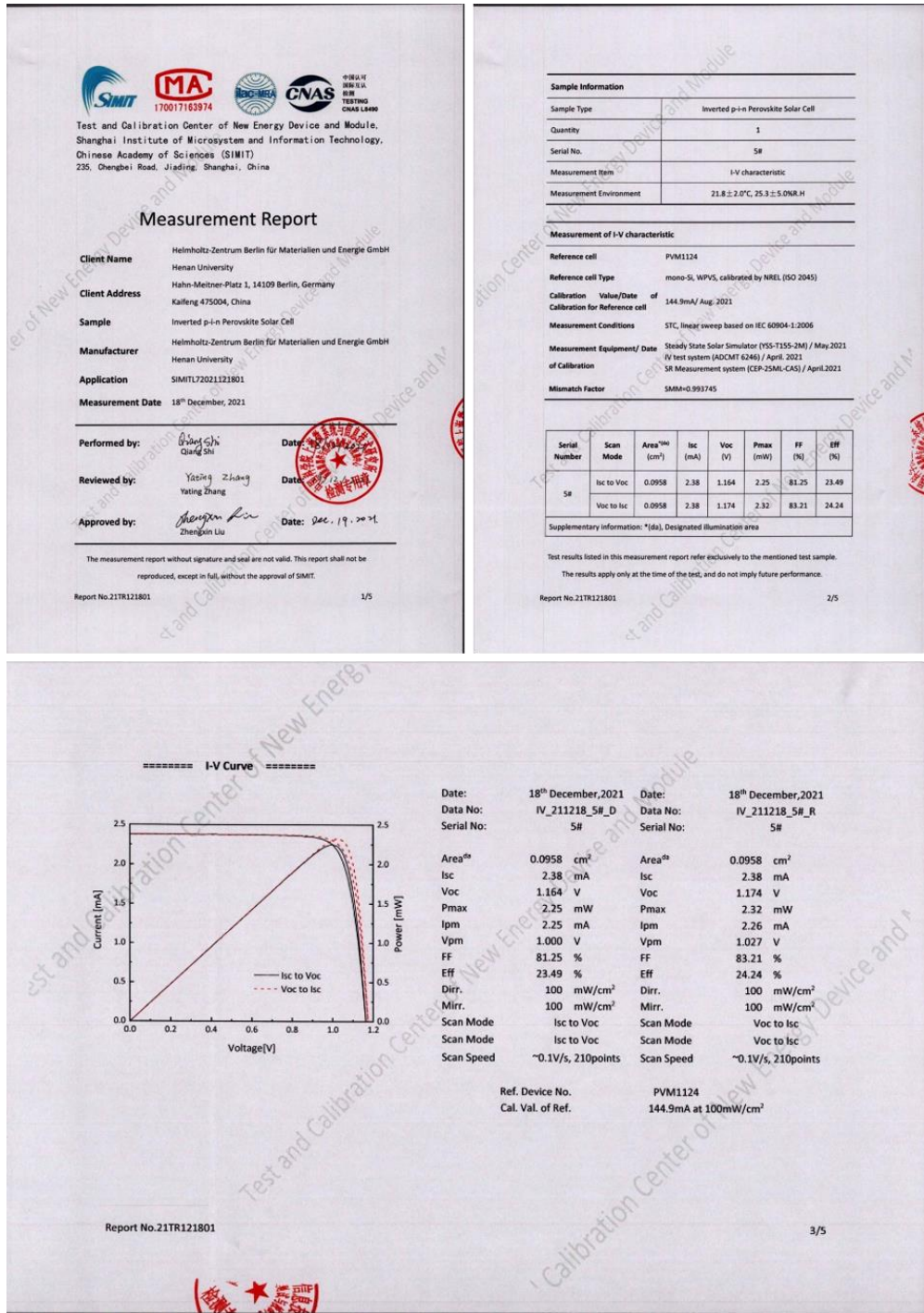
**Fig. S19.** Independent efficiency certification result of PSCs by an accredited institute of Test and Calibration Center of New Energy Device and Module, Shanghai Institute of Microsystem and Information Technology, Chinese Academy of Sciences (SIMIT).

We obtained a certified PCE of 24.24% from SIMIT with $J_{sc}$ of 24.84 mA/cm$^2$, $V_{oc}$ of 1.174 V and FF of 83.21% under an aperture area of 9.58 mm$^2$ (**Fig. S19**), further supporting our results.
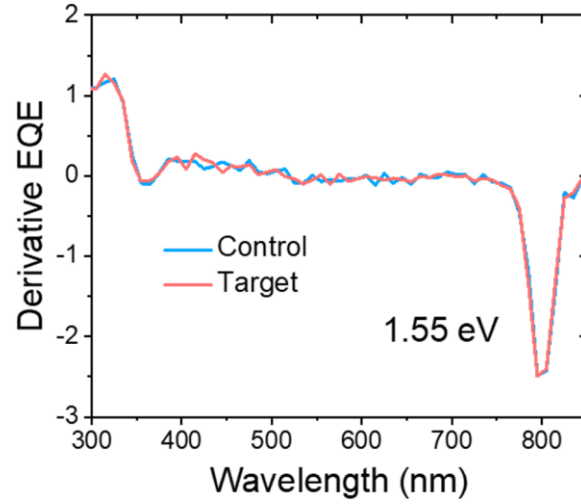
**Fig. S20.** Bandgap of perovskite layers calculated from the intercept of the EQE spectra.

The bandgap of control and target perovskite layers is determined from the derivative EQE spectrum (**Fig. S20**), which of both are about 1.55 eV. It indicates that the $\beta$-pV2F's optimisation did not change the material bandgap.
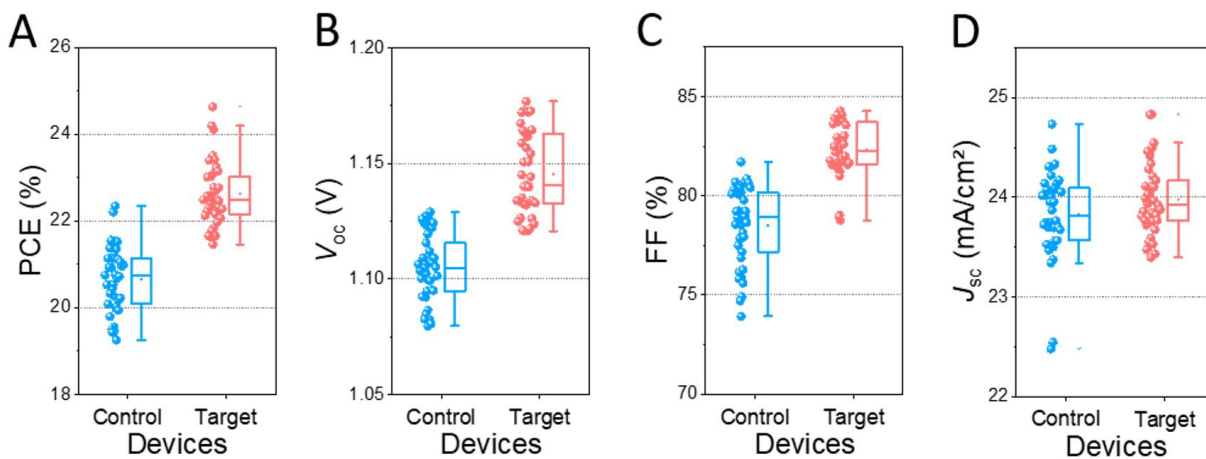
**Fig. S21.** The statistics of (**A**) PCE, (**B**) $V_{oc}$, (**C**) FF and (**D**) $J_{sc}$ distribution for control and target devices.
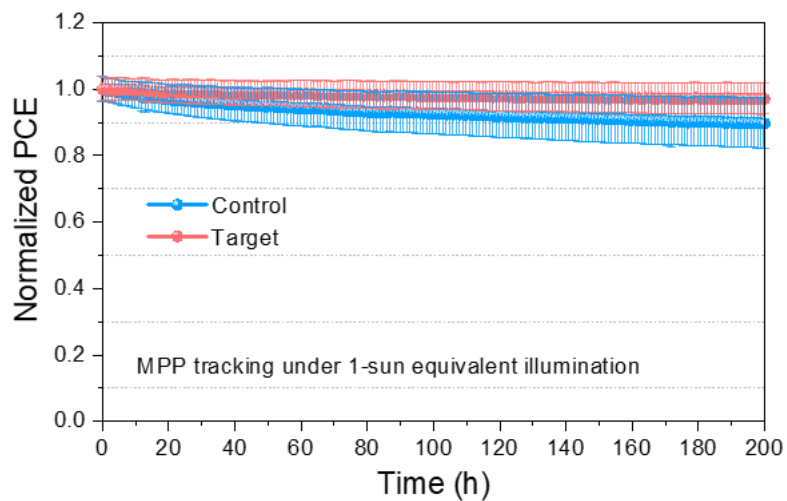
**Fig. S22.** Statistical operational stability of unencapsulated control and target devices ($n = 12$) tracking under continuous illumination in $N_2$ atmosphere.
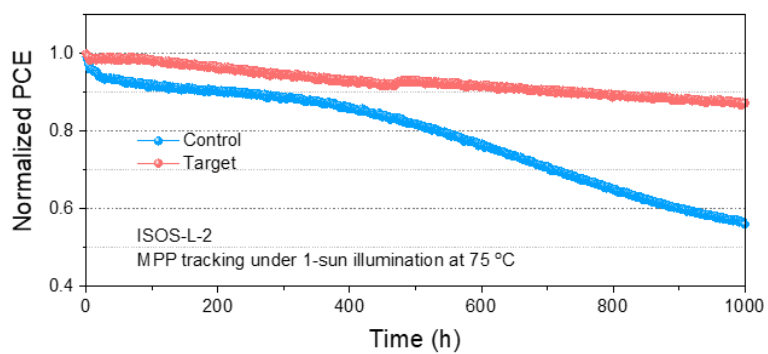
**Fig. S23.** Normalized PCEs of unencapsulated PSCs as a function of time measured at MPP under continuous illumination in an $N_2$ atmosphere at 75 °C.
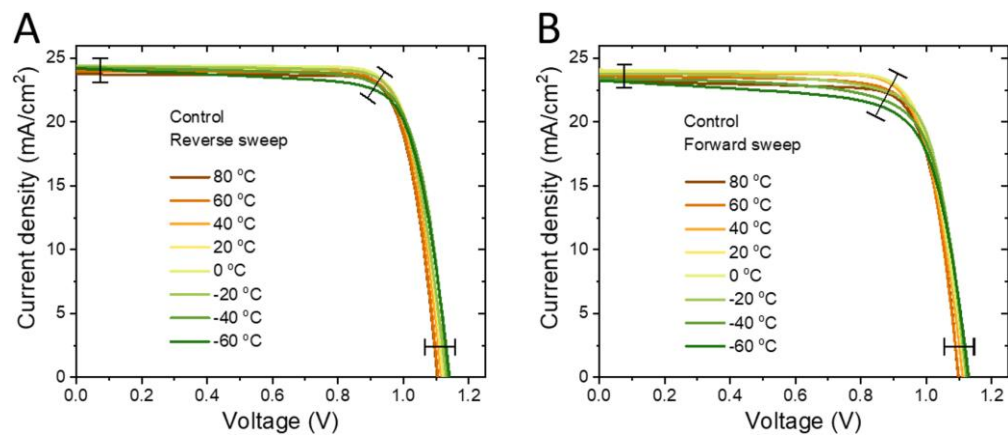
**Fig. S24.** The (**A**) reversed-scanned and (**B**) forward-scanned *J-V* characteristics of typical control PSC during thermal cycles.
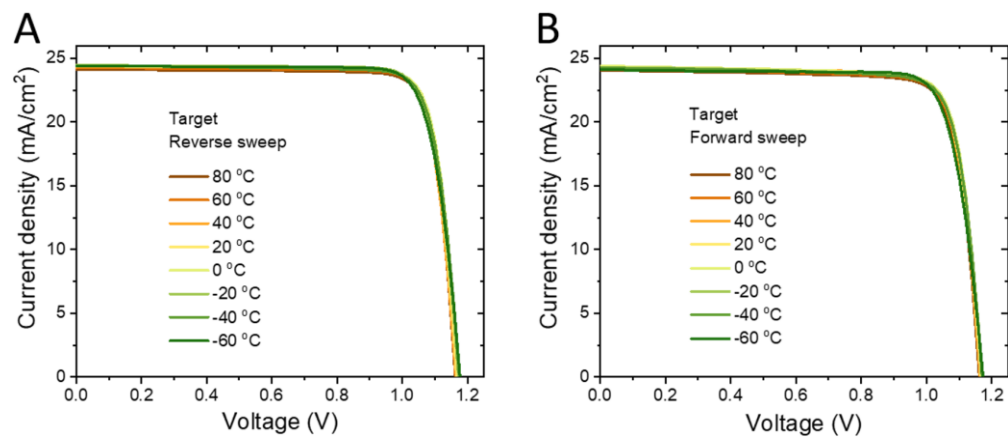
**Fig. S25.** The (**A**) reversed-scanned and (**B**) forward-scanned *J-V* characteristics of typical target PSC during thermal cycles.
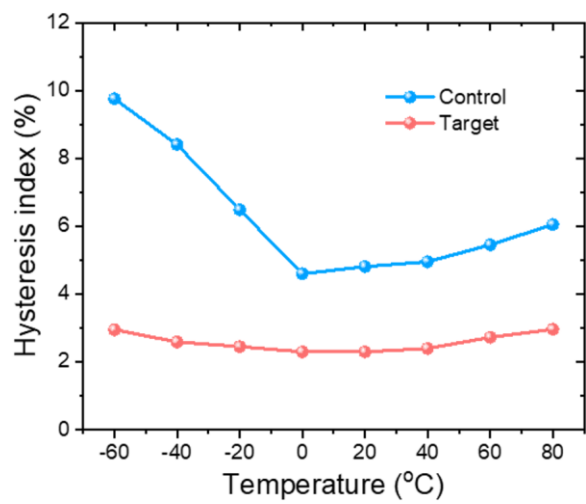
**Fig. S26.** The hysteresis index evolution against thermal cycles of control and target PSCs.
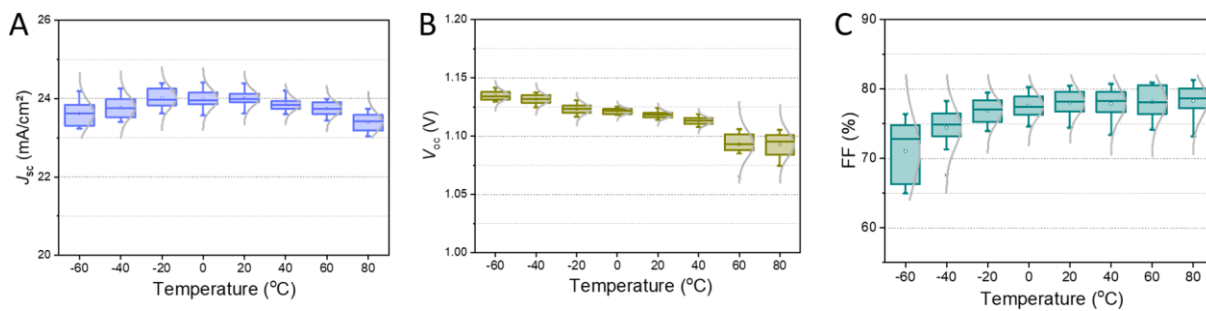
**Fig. S27.** Statistical temperature-dependence profiles of (**A**) $J_{sc}$, (**B**) $V_{oc}$, and (**C**) FF for control PSCs.
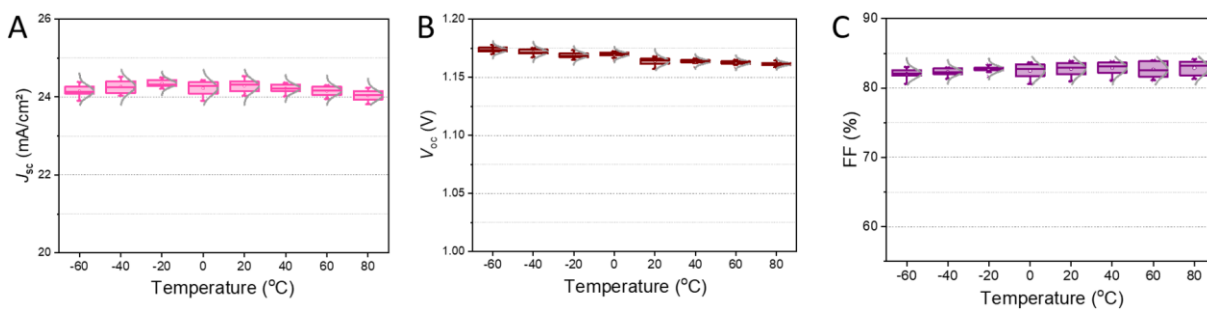
**Fig. S28.** Statistical temperature-dependence profiles of (**A**) $J_{sc}$, (**B**) $V_{oc}$, and (**C**) FF for target PSCs.
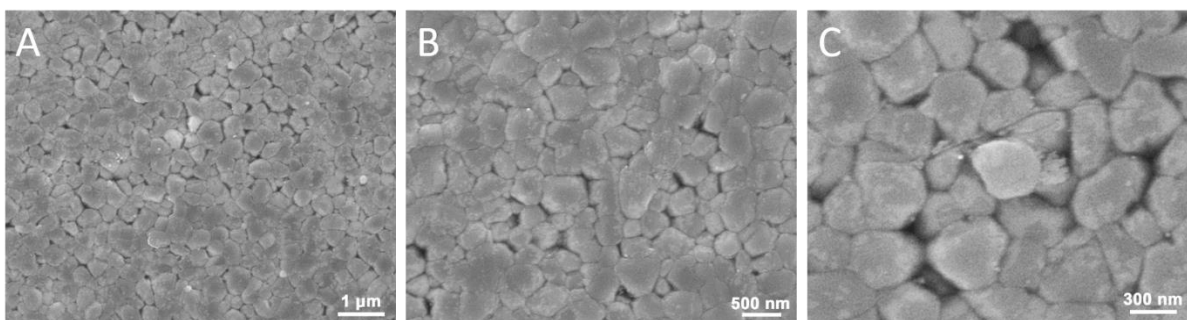
**Fig. S29.** Top-view SEM images of the control films aged by simulated thermal cycling operation. The film ageing is proceeded with the same process as the thermal cycling of the device. (There is a 20 °C/min ramp rate for rapid thermal cycling between −60 °C and +80 °C for 120 cycles, with an extra 2 minutes waiting windows for thermal equilibrium at −60 °C and +80 °C. The temperature starts from room temperature heating to +80 °C and then cooling to −60 °C. The progress ends at room temperature. The time per complete cycle is 18 min.)

After thermal cycling aging, control perovskites showed severe morphological degradation (**Fig. S29**).
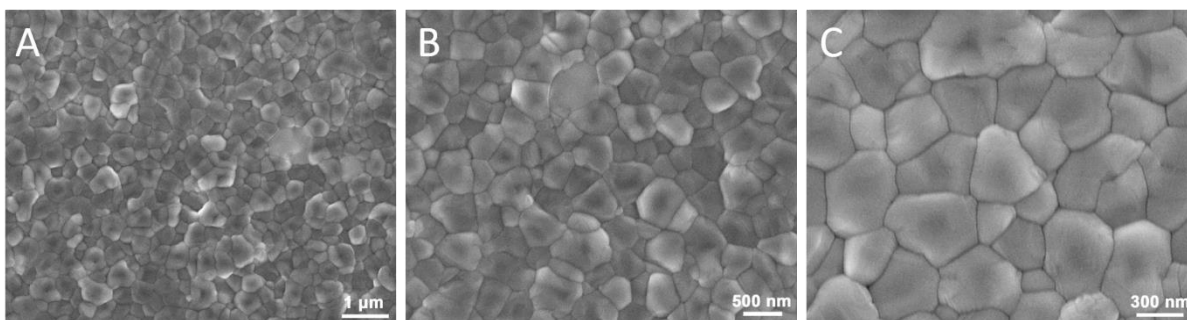
**Fig. S30.** Top-view SEM images of the target films with *β*-pV2F treatment aged by simulated thermal cycling operation. (There is a 20 °C/min ramp rate for rapid thermal cycling between −60 °C and +80 °C for 120 cycles, with an extra 2 minutes waiting windows for thermal equilibrium at −60 °C and +80 °C. The temperature starts from room temperature heating to +80 °C and then cooling to −60 °C. The progress ends at room temperature. The time per complete cycle is 18 min.)

As presented in **Fig. S30**, no obvious change in morphology was found for aged target perovskites.
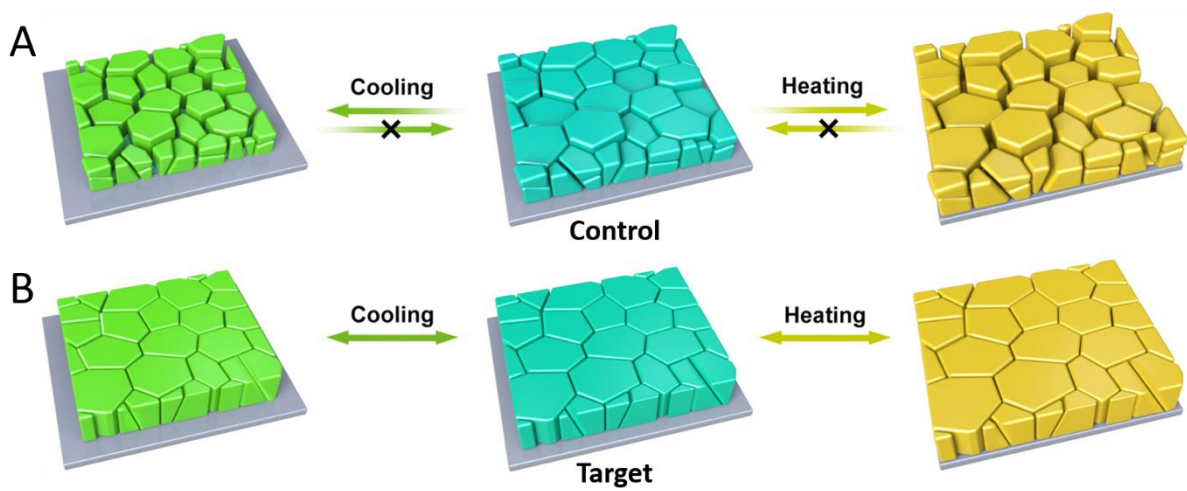
**Fig. S31.** Schematic of (**A**) control and (**B**) target perovskites aged with simulated thermal cycling.
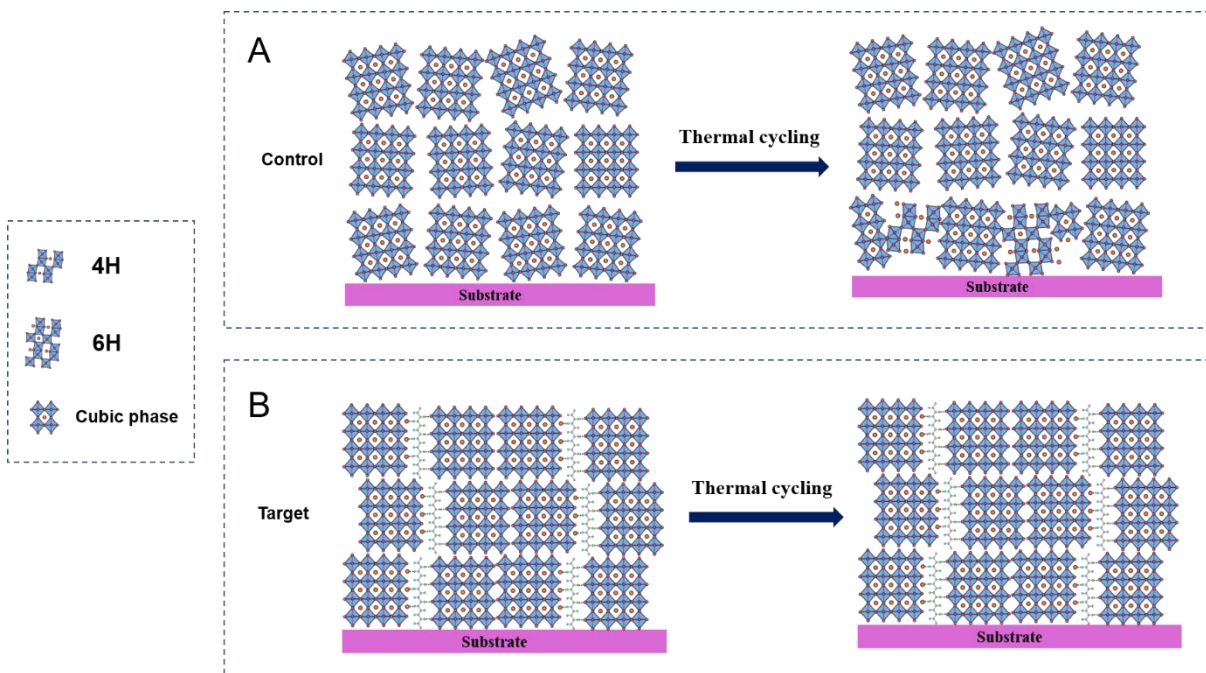
**Fig. S32.** Phase transition schematic of (**A**) control and (**B**) target perovskites during thermal cycling.
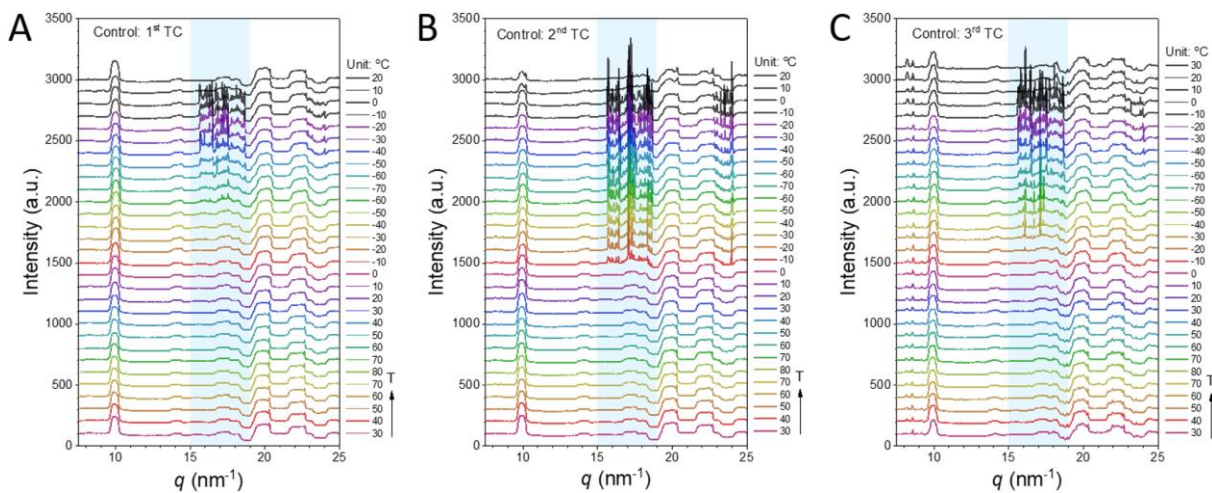
**Fig. S33.** The azimuthally integrated intensity during (**A**) first, (**B**) second and (**C**) third thermal cycles for control perovskite.
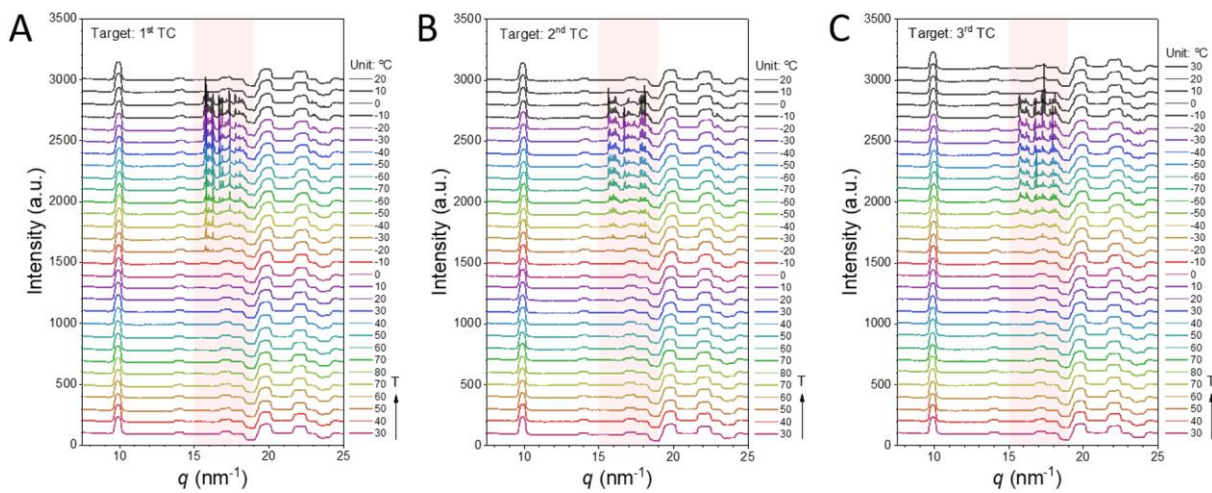
**Fig. S34.** The azimuthally integrated intensity during (**A**) first, (**B**) second and (**C**) third thermal cycles for target perovskite.
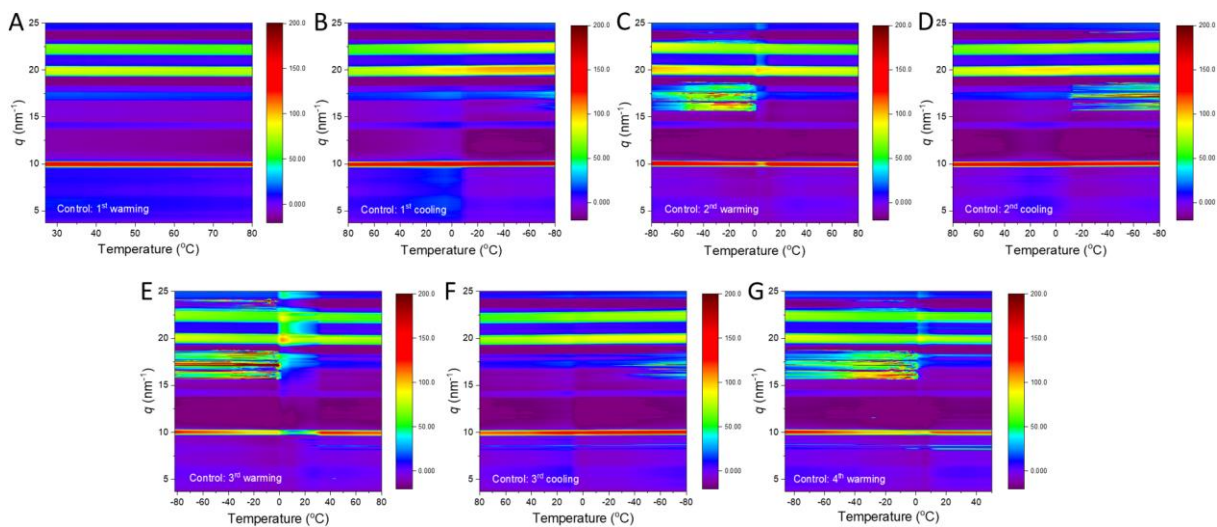
**Fig. S35.** The false-color intensity maps versus *q* and temperatures from the *in situ* GIWAXS measurement of control perovskite carried out during (**A**) first warming cycle, (**B**) first cooling cycle, (**C**) second warming cycle, (**D**) second cooling cycle, (**E**) third warming cycle, (**F**) third cooling cycle, and (**G**) forth warming cycle processes.
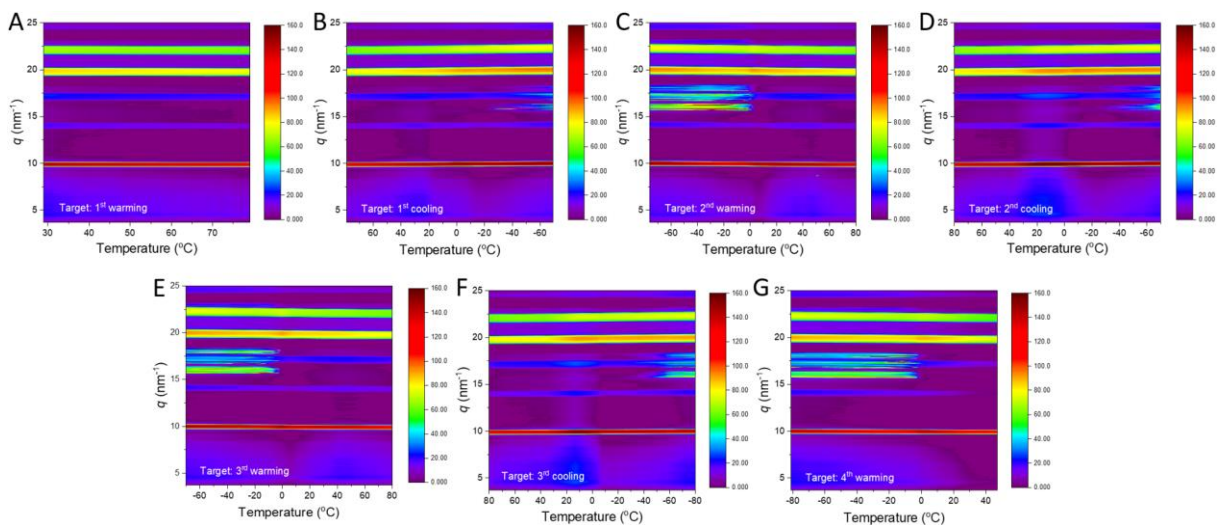
**Fig. S36.** The false-color intensity maps versus *q* and temperatures from the *in situ* GIWAXS measurement of target perovskite carried out during (**A**) first warming cycle, (**B**) first cooling cycle, (**C**) second warming cycle, (**D**) second cooling cycle, (**E**) third warming cycle, (**F**) third cooling cycle, and (**G**) forth warming cycle processes.
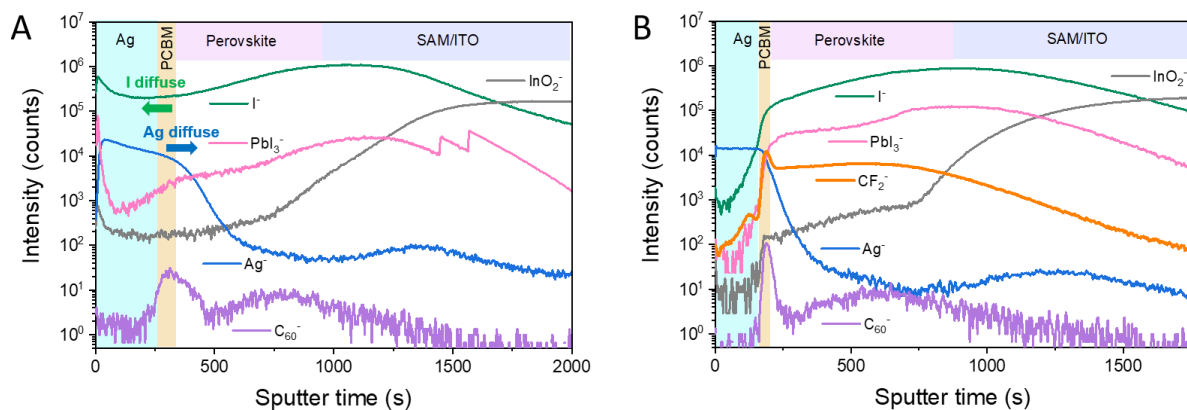
**Fig. S37.** ToF-SIMS ion species depth profiles of $Ag^-$ (Ag), $C_{60}^-$ (PCBM), $I^-$, $PbI_3^-$ (perovskite), $CF_2^-$ ($\beta$-pV2F), and $InO_2^-$ (ITO) of the aged (**A**) control and (**B**) target devices after thermal cycling.

From ToF-SIMS ion species depth profiles in **Fig. S37**, we observe ion migration occurred in the control device and suppressed in the target device. In target PSCs, $\beta$-pV2F is mainly distributed on the interface between perovskite and PCBM (**Fig. S37B**), where the polymer interlayer contributes to cut off ion migration route in addition to stabilized crystal structure by optimizing crystallization.
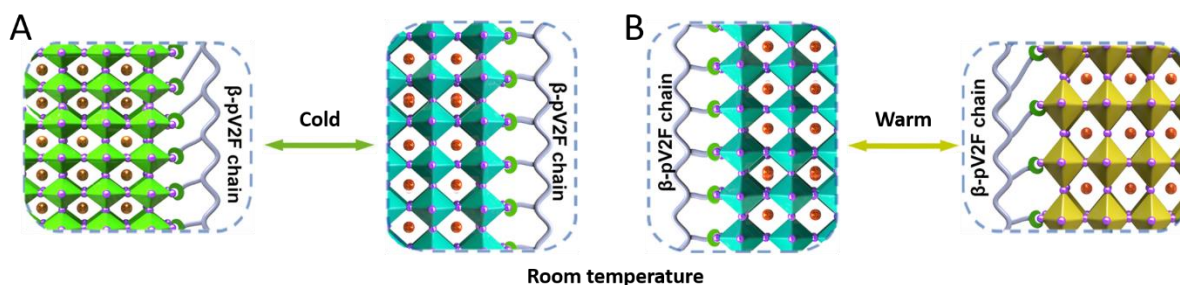
**Fig. S38.** The strain release mechanism in target perovskite with temperature changes.

The positively charged -CH$_2$ dipoles on the long-chain $\beta$-pV2F molecule bind the perovskite halogen, dominating the release of the perovskite lattice strain. As shown in **Fig. S38**, the long-chain interfacial interaction can release the strain of the inorganic [PbI$_6$]$^{4-}$ octahedron skeleton by pulling during changing temperatures. Due to the reduced lattice strain, the perovskite phase stability is improved.
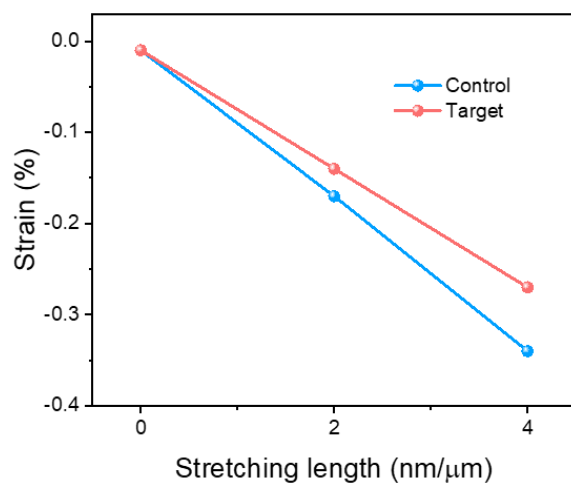
**Fig. S39.** The strain as a function of stretching lengths. (The strain (%) is calculated by dividing the $q$ difference ($\Delta q$) by the $q$ value.)

Reporting the strain as a function of stretching length (**Fig. S39**), we can observe that the polymer's introduction reduces the strain generation of perovskites during stretching.

## Supplementary Tables

**Table S1.** Summarized photovoltaic parameters extracted from the reverse and forward *J-V* curves of control PSCs at different temperatures.

| Temperature (°C) | Sweep | $J_{sc}$ (mA/cm$^2$) | $V_{oc}$ (V) | FF (%) | PCE (%) | HI (%) |
|---|---|---|---|---|---|---|
| 80 | Reverse | 23.73 | 1.104 | 80.9 | 21.2 | 6.05 |
|    | Forward | 23.22 | 1.098 | 78.1 | 19.9 |      |
| 60 | Reverse | 23.98 | 1.106 | 80.6 | 21.4 | 5.45 |
|    | Forward | 23.61 | 1.099 | 77.9 | 20.2 |      |
| 40 | Reverse | 24.21 | 1.116 | 80.3 | 21.7 | 4.95 |
|    | Forward | 23.82 | 1.112 | 77.9 | 20.6 |      |
| 20 | Reverse | 24.38 | 1.121 | 80.0 | 21.9 | 4.81 |
|    | Forward | 24.00 | 1.116 | 77.7 | 20.8 |      |
| 0  | Reverse | 24.41 | 1.125 | 79.6 | 21.9 | 4.60 |
|    | Forward | 24.08 | 1.120 | 77.3 | 20.9 |      |
| −20 | Reverse | 24.39 | 1.131 | 78.8 | 21.7 | 6.49 |
|     | Forward | 23.80 | 1.123 | 76.0 | 20.3 |      |
| −40 | Reverse | 24.26 | 1.137 | 77.0 | 21.2 | 8.41 |
|     | Forward | 23.40 | 1.127 | 73.8 | 19.5 |      |
| −60 | Reverse | 24.19 | 1.142 | 75.6 | 20.9 | 9.76 |
|     | Forward | 23.23 | 1.130 | 71.7 | 18.8 |      |

**Table S2.** Summarized photovoltaic parameters extracted from the reverse and forward *J-V* curves of target PSCs at different temperatures.

| Temperature (°C) | Sweep | $J_{sc}$ (mA/cm$^2$) | $V_{oc}$ (V) | FF (%) | PCE (%) | HI (%) |
|---|---|---|---|---|---|---|
| 80 | Reverse | 24.12 | 1.163 | 84.1 | 23.6 | 2.96 |
|    | Forward | 24.07 | 1.162 | 81.9 | 22.9 |      |
| 60 | Reverse | 24.26 | 1.164 | 84.0 | 23.7 | 2.73 |
|    | Forward | 24.16 | 1.164 | 82.1 | 23.1 |      |
| 40 | Reverse | 24.36 | 1.165 | 83.8 | 23.8 | 2.40 |
|    | Forward | 24.33 | 1.164 | 82.0 | 23.2 |      |
| 20 | Reverse | 24.40 | 1.168 | 83.6 | 23.8 | 2.30 |
|    | Forward | 24.40 | 1.165 | 81.9 | 23.3 |      |
| 0  | Reverse | 24.43 | 1.172 | 83.4 | 23.9 | 2.30 |
|    | Forward | 24.40 | 1.170 | 81.8 | 23.3 |      |
| −20 | Reverse | 24.45 | 1.173 | 82.9 | 23.8 | 2.45 |
|     | Forward | 24.28 | 1.171 | 81.6 | 23.2 |      |
| −40 | Reverse | 24.41 | 1.175 | 82.8 | 23.8 | 2.59 |
|     | Forward | 24.28 | 1.172 | 81.3 | 23.1 |      |
| −60 | Reverse | 24.39 | 1.178 | 82.5 | 23.7 | 2.95 |
|     | Forward | 24.12 | 1.174 | 81.2 | 23.0 |      |

**Table S3.** Summary of the lattice strain for control and target perovskites under first thermal cycling.

| Thermal cycling | Temperature (°C) | Control strain (%) | Target strain (%) |
|---|---|---|---|
| | 30 | 0.090 | 0.070 |
| | 40 | 0.090 | 0.070 |
| | 50 | 0.030 | 0.071 |
| | 60 | 0.030 | 0.040 |
| | 70 | -0.010 | 0.030 |
| | 80 | -0.050 | -0.030 |
| | 70 | -0.010 | 0.000 |
| | 60 | 0.020 | 0.050 |
| | 50 | 0.020 | 0.071 |
| | 40 | 0.090 | 0.070 |
| | 30 | 0.090 | 0.080 |
| | 20 | 0.170 | 0.141 |
| | 10 | 0.220 | 0.221 |
| | 0 | 0.319 | 0.292 |
| | −10 | 0.339 | 0.301 |
| | −20 | 0.339 | 0.301 |
| | −30 | 0.359 | 0.291 |
| First TC | −40 | 0.429 | 0.290 |
| | −50 | 0.498 | 0.290 |
| | −60 | 0.527 | 0.330 |
| | −70 | 0.567 | 0.360 |
| | −60 | 0.468 | 0.310 |
| | −50 | 0.438 | 0.280 |
| | −40 | 0.369 | 0.290 |
| | −30 | 0.349 | 0.291 |
| | −20 | 0.259 | 0.221 |
| | −10 | 0.150 | 0.150 |
| | 0 | 0.120 | 0.100 |
| | 10 | 0.080 | 0.060 |
| | 20 | 0.060 | 0.070 |
| | 30 | 0.020 | 0.060 |

**Table S4.** Summary of the lattice strain for control and target perovskites under second thermal cycling.

| Thermal cycling | Temperature (°C) | Control strain (%) | Target strain (%) |
|---|---|---|---|
| | 30 | 0.020 | 0.060 |
| | 40 | 0.010 | 0.000 |
| | 50 | -0.010 | -0.020 |
| | 60 | 0.020 | -0.020 |
| | 70 | -0.020 | -0.050 |
| | 80 | -0.120 | -0.061 |
| | 70 | -0.070 | -0.050 |
| | 60 | -0.030 | 0.000 |
| | 50 | -0.030 | 0.000 |
| | 40 | 0.040 | 0.060 |
| | 30 | 0.050 | 0.081 |
| | 20 | 0.080 | 0.141 |
| | 10 | 0.140 | 0.221 |
| | 0 | 0.170 | 0.292 |
| | −10 | 0.200 | 0.302 |
| | −20 | 0.220 | 0.301 |
| | −30 | 0.269 | 0.301 |
| Second TC | −40 | 0.319 | 0.291 |
| | −50 | 0.349 | 0.290 |
| | −60 | 0.418 | 0.350 |
| | −70 | 0.478 | 0.360 |
| | −60 | 0.418 | 0.340 |
| | −50 | 0.379 | 0.290 |
| | −40 | 0.309 | 0.291 |
| | −30 | 0.259 | 0.281 |
| | −20 | 0.189 | 0.221 |
| | −10 | 0.130 | 0.150 |
| | 0 | 0.110 | 0.141 |
| | 10 | 0.060 | 0.070 |
| | 20 | 0.010 | 0.060 |
| | 30 | 0.030 | 0.060 |

**Table S5.** Summary of the lattice strain for control and target perovskites under third thermal cycling.

| Thermal cycling | Temperature (°C) | Control strain (%) | Target strain (%) |
|---|---|---|---|
| | 30 | 0.030 | 0.060 |
| | 40 | 0.020 | 0.020 |
| | 50 | 0.000 | 0.010 |
| | 60 | -0.020 | 0.010 |
| | 70 | -0.060 | -0.030 |
| | 80 | -0.130 | -0.030 |
| | 70 | -0.060 | -0.030 |
| | 60 | -0.020 | 0.010 |
| | 50 | 0.050 | 0.030 |
| | 40 | 0.070 | 0.050 |
| | 30 | 0.090 | 0.121 |
| | 20 | 0.110 | 0.151 |
| | 10 | 0.140 | 0.221 |
| | 0 | 0.200 | 0.282 |
| | −10 | 0.230 | 0.291 |
| | −20 | 0.280 | 0.291 |
| | −30 | 0.320 | 0.321 |
| Third TC | −40 | 0.369 | 0.341 |
| | −50 | 0.399 | 0.361 |
| | −60 | 0.438 | 0.360 |
| | −70 | 0.478 | 0.380 |
| | −60 | 0.410 | 0.360 |
| | −50 | 0.339 | 0.360 |
| | −40 | 0.289 | 0.341 |
| | −30 | 0.219 | 0.341 |
| | −20 | 0.189 | 0.311 |
| | −10 | 0.150 | 0.241 |
| | 0 | 0.120 | 0.181 |
| | 10 | 0.090 | 0.100 |
| | 20 | 0.030 | 0.070 |
| | 30 | -0.070 | 0.070 |

**Supplementary References**

45. S. N. Habisreutinger, N. K. Noel, H. J. Snaith, Hysteresis Index: A Figure without Merit for Quantifying Hysteresis in Perovskite Solar Cells. *ACS Energy Lett.* **3**, 2472-2476 (2018).
46. H. Wang *et al.*, Interfacial Residual Stress Relaxation in Perovskite Solar Cells with Improved Stability. *Adv. Mater.* **31**, 1904408 (2019).
47. N. Rolston *et al.*, Engineering Stress in Perovskite Solar Cells to Improve Stability. *Adv. Energy Mater.* **8**, 1802139 (2018).
48. M. A. Reyes-Martinez *et al.*, Time-Dependent Mechanical Response of APbX3 (A = Cs, CH3NH3; X = I, Br) Single Crystals. *Adv. Mater.* **29**, 1606556 (2017).
49. J. Yu, M. Wang, S. Lin, Probing the Soft and Nanoductile Mechanical Nature of Single and Polycrystalline Organic–Inorganic Hybrid Perovskites for Flexible Functional Devices. *ACS Nano* **10**, 11044-11057 (2016).
50. S. K. Karan *et al.*, Designing high energy conversion efficient bio-inspired vitamin assisted single-structured based self-powered piezoelectric/wind/acoustic multi-energy harvester with remarkable power density. *Nano Energy* **59**, 169-183 (2019).
51. A. Tamang *et al.*, DNA-Assisted β-phase Nucleation and Alignment of Molecular Dipoles in PVDF Film: A Realization of Self-Poled Bioinspired Flexible Polymer Nanogenerator for Portable Electronic Devices. *ACS Appl. Mater. Interfaces* **7**, 16143-16147 (2015).
52. M. Wang *et al.*, Small Molecule Modulator at the Interface for Efficient Perovskite Solar Cells with High Short-Circuit Current Density and Hysteresis Free. *Adv. Electron. Mater.* **6**, 2000604 (2020).